Magnetic Resonance in Medicine 74:396–409 (2015)

# Monitoring, Analysis, and Correction of Magnetic Field Fluctuations in Echo Planar Imaging Time Series

Lars Kasper,[1,2*†] Saskia Bollmann,[1†] S. Johanna Vannesjo,[1] Simon Gross,[1] Maximilian Haeberlin,[1] Benjamin E. Dietrich,[1] and Klaas P. Pruessmann[1]

**Purpose:** To assess the utility of concurrent magnetic field monitoring for observing and correcting for variations in k-space trajectories and global background fields that occur in single-shot echo planar imaging (EPI) time series as typically used in functional MRI (fMRI).
**Methods:** Field monitoring was performed using an array of NMR field probes operated concurrently with series of single-shot EPI acquisitions from a static phantom. The observed fluctuations in field evolution were analyzed in terms of their temporal and spatial behavior at the field level as well as at the level of reconstructed image series. The potential to correct for such fluctuations was assessed by accounting for them upon image reconstruction. An indication of the number and relative magnitude of underlying effects was obtained via principal component analysis.
**Results:** Trajectory and global field variations were found to induce substantial image fluctuations. Global field fluctuations induced standard deviations in image intensity up to 31%. Fluctuations in the trajectory induced ghosting artifacts with standard deviations up to 2%. Concurrent magnetic field monitoring reduced the fluctuations in the EPI time series to a maximum of 1.2%.
**Conclusion:** Concurrent magnetic field monitoring holds the potential to improve the net sensitivity of fMRI by reducing signal fluctuations unrelated to brain activity. **Magn Reson Med 74:396–409, 2015. © 2014 Wiley Periodicals, Inc.**

**Key words:** fMRI; gradients; noise; SFNR; thermal drifts; PCA

## INTRODUCTION

In functional MRI (fMRI), image time series are acquired to analyze brain activity–related signal fluctuations in each voxel over many scans. The targeted changes in image intensity over the course of the experiment are induced by blood oxygenation level–dependent (BOLD) or perfusion signal fluctuations (1,2). However, fluctuations in the magnetic fields encoding the images induce signal fluctuations in the image time series as well. These encoding field fluctuations can be caused by a wide range of object-independent effects, such as instabilities in the gradient system, eddy current fluctuations in the cryostat, the main magnet and the shim coils, atmospheric pressure variations, changes in the cryogen level, and heating (3–7). Furthermore, the imaged object itself can induce field fluctuations, such as those due to breathing (8–10). These unwanted signal fluctuations lead to confounds and sensitivity loss in the image time series analysis.

Thus far, reproducible deviations from ideal encoding fields within one readout have been addressed thoroughly in the literature, and many correction methods have been proposed (e.g., (3,4,11,12)). However, fluctuations in encoding fields, which we define here as the variability of the encoding fields between readouts, are typically not addressed. One prominent exception is navigators, which partially enable dynamic corrections by assessing field fluctuations using point-wise measurements between scans (5,8,13,14) even up to second order in space (15). Because these point-wise measurements are not taken during the actual encoding, the capability of correcting fluctuations in the encoding fields is limited to frequency shifts in the magnetic field. Furthermore, additional measurements are required that alter the MR sequence and the timing of the data acquisition.

Recently, magnetic field monitoring using NMR field probes was introduced as a means to measure and correct for spatio-temporal magnetic field fluctuations (6,16,17). Specifically, magnetic field monitoring enables to study the complete evolution of the encoding fields concurrently (18) with the imaging process and without any alterations to the imaging sequence itself. This opens up the opportunity to follow encoding field fluctuations over different time scales and quantify their contribution to image fluctuations. Furthermore, it also enables a general correction method for measured field fluctuations upon image reconstruction (19).

In this study, we used concurrent magnetic field monitoring to study and correct for fluctuations in the encoding fields of a typical echo planar imaging (EPI) trajectory common to fMRI experiments. In particular, we compared fluctuations over different time scales, i.e., between different scans of a session, between different sessions within a day, and between different days. We focused on phantom experiments exclusively to eliminate confounds related to subject physiology (e.g., breathing and cardiovascular mechanisms). First, we measured field fluctuations both in the global phase evolution as well as the imaging trajectory itself. Second, we quantified the effects of these field fluctuations on image

[1]Institute of Biomedical Engineering, University of Zurich and ETH Zurich, Zurich, Switzerland.
[2]Translational Neuromodeling Unit, Institute for Biomedical Engineering, University of Zurich and ETH Zurich, Zurich, Switzerland.
Grant sponsor: Swiss Commission for Technology and Innovation; Grant number: 13756.1 PFFLM-NM. Grant sponsor: Swiss National Competence Center for Bioimaging; PhD Fellowship (M.H.).
*Correspondence to: Lars Kasper, Institute for Biomedical Engineering, Gloriastrasse 35, 8092 Zurich, Switzerland. E-mail: kasper@biomed.ee.ethz.ch
†These authors contributed equally to this work.
Received 31 March 2014; revised 21 July 2014; accepted 22 July 2014
DOI 10.1002/mrm.25407
Published online 14 August 2014 in Wiley Online Library (wileyonlinelibrary.com).
 

Table 1
Measurement Protocol

| | Session 1 | | Session 2 | | Session 3 |
|---|---|---|---|---|---|
| Day 1 | Set 1 | Break | Set 2 | Break | Set 3 |
| Day 2 | Set 4 | Break | Set 5 | Break | Set 6 |
| Day 3 | Set 7 | Break | Set 8 | Break | Set 9 |
| | 20 min | 20 min | 20 min | 20 min | 20 min |

Each set contained 400 EPI volumes with a volume repetition time (TR) of 3 s.

reconstruction by comparing images reconstructed with and without fluctuation correction. Finally, we applied principal component analysis as a data-driven approach to explore characteristic fluctuations in the encoding fields and the characteristic image fluctuations they induce.

## METHODS

### Hardware Setup

All experiments were performed on a Philips Achieva 3T system (Philips Healthcare, Best, The Netherlands) using an eight-channel head coil array. Field monitoring was performed with an array of 12 unshielded transmit/receive field probes (6,16,17) (inner diameter: 0.8 mm, $T_1 \approx 100$ ms, $T_2^* \approx 50$ ms) using $^{19}$F-NMR for operation concurrent with imaging readouts (19). The probes were excited using a 90° block pulse. For data acquisition, the scanner spectrometer was used with an analog-to-digital converter dwell time of 2.66 μs. The probes were attached to the inner surface of the head coil (22.6 cm diameter), distributed approximately evenly on a cylindrical surface for suitable conditioning of field expansions (16).

### Field Monitoring

#### *Phase Coefficients*

For monitoring imaging readouts, the field probes were excited before the EPI prephaser gradient and read out continuously during the subsequent acquisition of image data. The probe signals were processed as described previously (16), including demodulation by the predetermined local frequency offset of each probe, phase extraction, and unwrapping. The 12 phase time courses were then expanded into second-order spherical harmonics comprising a total of nine spatial terms. In this expansion, the zeroth-order term, $k_0(t)$, reflects phase accrued due to global, spatially uniform field variation whereas the first-order terms, $\boldsymbol{k} = k_x(t),\ k_y(t),\ k_z(t)$, reflect phase accrual of first-order in space according to the common k-space formalism. Since all scans were of transverse orientation, of the trajectory $\boldsymbol{k}(t)$ only $k_x(t)$ and $k_y(t)$ were considered for reconstruction. For more compact nomenclature, they are jointly referred to as $\boldsymbol{k_{x,y}}(t)$ here. The second-order terms were neglected at the reconstruction level since they cannot be accounted for by mere Fourier reconstruction. Higher-order reconstruction is feasible (19) but incurs substantially greater computational demand, thus it was not employed in this study, aiming to establish the impact only of the dominant zeroth- and first-order fluctuations. The latter were determined with a second-order field model nevertheless to prevent bias in the zeroth order, which is sensitive to aliasing even of minor second-order terms due to their enhanced magnitude at the peripheral probe positions.

#### *Noise in Probe Readouts*

The sensitivity of the field probes is described by their signal-to-noise ratio times the root of the acquisition bandwidth (6). In the absence of encoding gradients, this amounted to $4.8 \cdot 10^4\sqrt{\text{Hz}}$ and $2.6 \cdot 10^4\sqrt{\text{Hz}}$ at the beginning and end of the readout, respectively. In the presence of the EPI gradient sequence, these values decreased only slightly to $4.4 \cdot 10^4\sqrt{\text{Hz}}$ after the prephaser and $2.4 \cdot 10^4\sqrt{\text{Hz}}$ at the end of the readout at maximum k-space excursion. At such high signal-to-noise ratios, the zero-mean Gaussian statistics of thermal noise translate into equally zero-mean Gaussian phase noise, whose magnitude increases with time due to signal decay. Phase noise statistics were thus determined in terms of their time-dependent noise covariance matrix $\boldsymbol{\Sigma}(t)$ calculated from a series of probe data time courses acquired in the absence of gradient operation. To eliminate potential variation by slow $B_0$ drifts, phase extraction and unwrapping was complemented by subtraction of any linear trend according to linear regression.

The propagation of probe noise into the phase coefficients $k_l$ ($l = 0,\ x,\ y$) depends on the conditioning of the probing matrix $\boldsymbol{P}$, which in turn depends on probe positioning (16). However, the generic condition number can be misleading, as it depends on the choice of length units in stating the entries of $\boldsymbol{P}$ for different spherical orders. Instead, noise propagation was analyzed explicitly as described previously (16,18). The covariance of the probe phase noise propagates into the phase coefficients as

$$\sigma_{k_l}^2(t) = (\boldsymbol{P}^{+}\boldsymbol{\Sigma}(t)\boldsymbol{P}^{+T})_{l,l} \qquad [1]$$

where + and $T$ indicate the Moore-Penrose pseudoinverse and matrix transposition, respectively. Equation [1] yielded $\sigma_{k_0} = 0.0065$ rad, $\sigma_{k_x} = 0.0716$ rad/m, and $\sigma_{k_y} = 0.0491$ rad/m at the beginning of the EPI readout and $\sigma_{k_0} = 0.0124$ rad, $\sigma_{k_x} = 0.1395$ rad/m, and $\sigma_{k_y} = 0.0854$ rad/m at the end of the EPI readout.

Knowledge of the covariance of probe phase noise was also used to generate equivalent synthetic noise for simulation purposes (cf. section simulations).

### Imaging Protocol

To study a typical fMRI scenario, single-shot two-dimensional EPI time series of a spherical water phantom (diameter 15 cm, doped with $CuSO_4$ to shorten $T_1$ relaxation) were acquired with the following parameters: volume repetition time = 3 s; echo time = 35 ms; EPI readout duration = 41.6 ms; bandwidth = 375 kHz; voxel size = 2.6 × 2.6 × 2.5 $mm^3$; field of view = 220 × 220 × 47.5 mm; 10 slices with a 2.5-mm interslice gap. Nine sets of such data were acquired on three different days with three imaging sessions on each day (Table 1). Each set contained 400 scans, amounting to a total duration of 20 min per set. Every set was followed by an equally long break (20 min) to mimic rest and preparation periods or the arrival of a new volunteer. For the determination of measurement error, a separate series of 120 readouts was performed with all probes simultaneously in the absence of gradient operation. Throughout data acquisition, interleaved $f_0$ determination and correction as well as the cold-head were turned off.

### Image Reconstruction

Image reconstruction was performed by inversion of the discretized MR signal equation:

$$s_\kappa = \sum_{\rho=1}^{N_\rho} m_\rho \cdot \exp\left(ik_0(t_k)\right) \cdot E_{\kappa,\rho} \qquad [2]$$

where $\boldsymbol{m} = (m_1, \cdots, m_\rho, \cdots, m_{N_\rho})$ represents the discretized object magnetization, $\kappa$, $\rho$ are index variables in time and space, respectively, and the Fourier encoding matrix $\boldsymbol{E}$ with entries $E_{\kappa,\rho} = \exp\left(i\boldsymbol{k}_{x,y}(t_\kappa) \cdot \boldsymbol{r}_\rho\right)$ comprises the effects of the first-order encoding fields.

First, for each receiver coil the signal $\boldsymbol{s} = (s_1, \cdots, s_\kappa, \cdots s_{N_\kappa})$ was demodulated with the global phase:

$$s_{demod,\kappa} = s_\kappa \cdot \exp\left(-ik_0(t_\kappa)\right) \qquad [3]$$

Individual single-coil image estimates $\hat{\boldsymbol{m}}$ were then computed via the Moore-Penrose pseudo-inverse of the encoding matrix (20):

$$\hat{\boldsymbol{m}} = (\boldsymbol{E}^H\boldsymbol{E})^{-1}\boldsymbol{E}^H\boldsymbol{s}_{demod}. \qquad [4]$$

The inversion operation was performed iteratively using the gridding-based conjugate-gradient method (20–22). A compound array image was then obtained by taking the root-sum-of-squares of the eight individual coil images. The image reconstructions as well as all further analysis steps were implemented in MATLAB (R2013a; The MathWorks, Inc., Natick, Massachusetts, USA).

### Reconstruction Schemes

To distinguish the impact of fluctuations and noise in $k_0(t)$ and $\boldsymbol{k}_{x,y}(t)$ and to study the feasibility of one-time calibration, several reconstruction schemes were implemented (Table 2). For the reference reconstruction, we incorporated concurrent monitoring information of zeroth and first order, i.e., $k_0(t)$ and $\boldsymbol{k}_{x,y}(t)$ (reconstruction scheme 1). In contrast, we reconstructed the image time series using no concurrent monitoring information, i.e., the mean over the 400 evolutions of $k_0(t)$ and $\boldsymbol{k}_{x,y}(t)$ observed in set 1 (reconstruction scheme 2). To better differentiate the underlying sources of fluctuations, in the subsequent analysis we investigated the effects of $k_0(t)$ and $\boldsymbol{k}_{x,y}(t)$ fluctuations separately. To investigate the effect of fluctuations in $k_0(t)$, its scan-dependent time series was replaced by a fixed mean over the 400 evolutions observed in set 1 while retaining the concurrently measured $\boldsymbol{k}_{x,y}(t)$ (reconstruction scheme 3). The converse strategy was employed to investigate the effect of fluctuations in $\boldsymbol{k}_{x,y}(t)$ (reconstruction scheme 4; Fig. 1B). Two further schemes served to study the utility of a calibration measurement that assumes reproducibility of the fluctuations in each set of 400 scans. Under this assumption, it suffices to measure the series of phase coefficient time courses of a single set (calibration) and use them to reconstruct other sets acquired in the same way. This approach, which we refer to as *session calibration*, was based on the 400 monitoring observations during set 1 and used to replace either the concurrent $k_0(t)$ (reconstruction scheme 5) or $\boldsymbol{k}_{x,y}(t)$ (reconstruction scheme 6) information for the other sets.

Table 2
Reconstruction Schemes

| Reconstruction scheme | Field information used for | |
|---|---|---|
| | $k_0$ | $\boldsymbol{k}_{x,y}$ |
| 1 Concurrent monitoring (reference) | $k_0(t)$ | $\boldsymbol{k}_{x,y}(t)$ |
| 2 Effect of $k_0$ and $\boldsymbol{k}_{x,y}$ fluctuations | $\bar{k}_0(t)\|_{set1}$ | $\bar{\boldsymbol{k}}_{x,y}(t)\|_{set1}$ |
| 3 Effect of $k_0$ fluctuations | $\bar{k}_0(t)\|_{set1}$ | $\boldsymbol{k}_{x,y}(t)$ |
| 4 Effect of $\boldsymbol{k}_{x,y}$ fluctuations | $k_0(t)$ | $\bar{\boldsymbol{k}}_{x,y}(t)\|_{set1}$ |
| 5 Effect of $k_0$ session calibration | $k_0(t)\|_{set1}$ | $\boldsymbol{k}_{x,y}(t)$ |
| 6 Effect of $\boldsymbol{k}_{x,y}$ session calibration | $k_0(t)$ | $\boldsymbol{k}_{x,y}(t)\|_{set1}$ |

Different reconstruction schemes were used to study fluctuations in the encoding fields and their correction. ($\bar{k}$ - average over the 400 volumes of set 1; $t$ - time within the EPI readout)

### Simulations

To distinguish the effects of field and trajectory fluctuations from other potential sources of image variation, such as fluctuations in the transmit or receive chain or mechanical vibrations of the phantom (23), data acquisition was simulated additionally based on the monitoring results. Synthetic data from a hypothetical single receiver coil was generated according to the discretized forward signal model (Eq. [2]). The numerical phantom of magnetization $\boldsymbol{m}$ was generated by taking the temporal mean of the actual phantom images of set 1 (Fig. 1A), which were reconstructed using the concurrently measured phase coefficients (reconstruction scheme 1) and with the background set to zero. Overall, we obtained 9 × 400 coil data time courses corresponding to the measured data, exclusively reflecting field fluctuations.

Synthetic data were also used to study the effect of probe noise on reconstructed images. To this end, simulated single-coil raw data was generated as described above using the average phase evolutions observed in set 1, $\overline{k_0}(t)$ and $\bar{\boldsymbol{k}}_{x,y}(t)$. Noisy probe data acquisition was emulated by starting from the underlying average probe phase time courses and adding synthetic noise of the previously determined probe noise covariance $\boldsymbol{\Sigma}(t)$ to 400 repetitions. The synthetic probe data was translated into

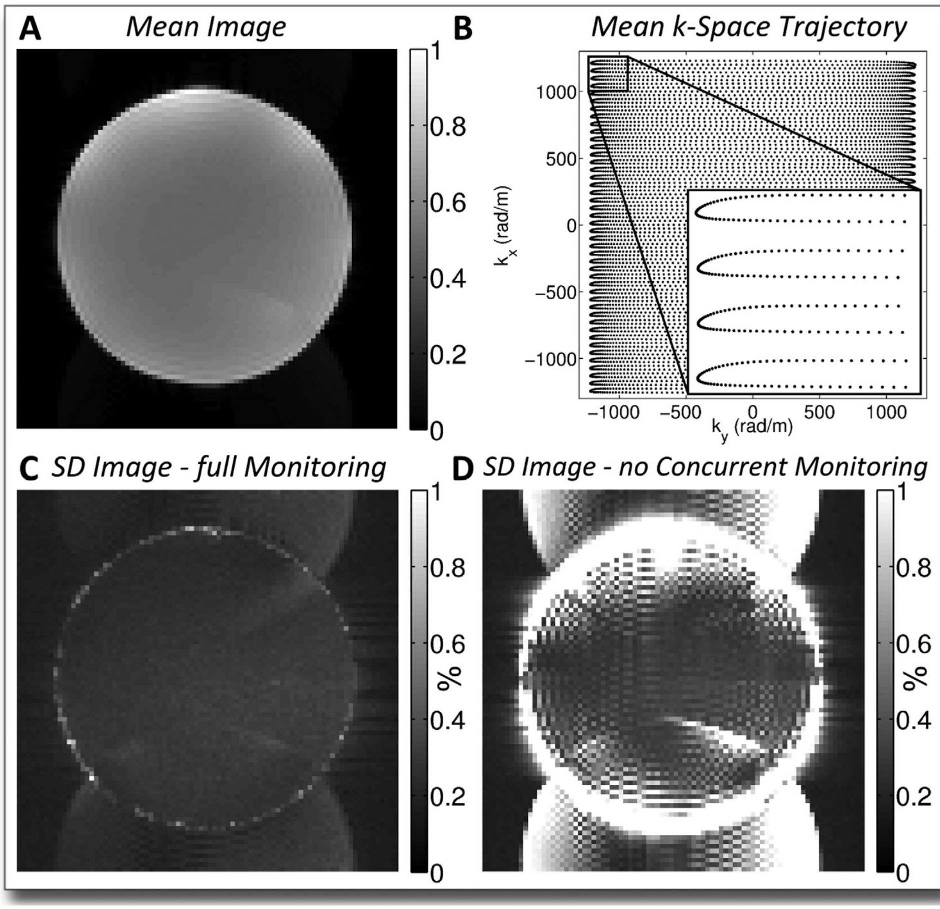


FIG. 1. **A**: Mean of the reconstructed images using the concurrently monitored phase coefficients for reconstruction (set 1, slice 9). **B:** Mean k-space trajectory (set 1, slice 9). **C:** Standard deviation (SD) image obtained using the concurrently monitored phase coefficients for reconstruction (set 1, slice 9). The SD is given as a percentage of the image intensity. **D:** SD image obtained using only the mean of the phase coefficients for reconstruction (i.e., the combined effect of $k_0$ and $\boldsymbol{k_{x,y}}$ fluctuations) (set 1, slice 9).

corresponding series of noise-bearing time courses of $k_0(t)$ and $\boldsymbol{k_{x,y}}(t)$. The propagation of probe noise into image fluctuations was then studied by using the series of noisy phase evolutions to reconstruct image time series from the synthetic raw image data. To distinguish the effects of noise in $k_0(t)$ and $\boldsymbol{k_{x,y}}(t)$, the noise-bearing series of each was combined with the respective noiseless counterpart in two separate simulations.

### Statistical Analysis of Image Fluctuations

We assessed the fluctuations within an EPI time series using standard deviation (SD) and root mean squared error (RMSE). The SD was computed for each voxel over the whole image time series within one set. Hence, the SD image provided a spatial depiction of the fluctuations and allowed the localization of areas with strong fluctuations. The image time series of each set were scaled such that the mean image spanned the range [0, 1]. Hence, the SD values, multiplied by 100, can be interpreted as percent signal change compared with BOLD imaging.

The RMSE, on the other hand, is computed for each individual image of the time series as the root mean squared difference to the reference image over all voxels. Thus, the RMSE quantifies the artifact level over the whole image. Furthermore, it provides a temporal fluctuation pattern and allows the identification of points in time with strong deviations. As the reference image for the estimation of the RMSE, we chose the mean image of the corresponding set reconstructed using the concurrently measured phase coefficients (reconstruction scheme 1). This allows for additional assessment of the overall artifact level given by a certain reconstruction scheme and prevents any stationary image artifacts to confound the statistics. For the simulated coil data, the numerical phantom (derived from Fig. 1A) served as the reference image.

Reflecting variation about mean pixel values, the SD can be regarded as a measure of precision in the image time series, which in turn is crucial for BOLD sensitivity. The RMSE, on the other hand, reflects image deviation from the highest-accuracy reconstruction available or, in the case of the simulations, from the actual ground truth. It can therefore be interpreted as a measure of image accuracy, which plays an important role in effect localization.

### Data-Driven Time Series Analysis: Principal Component Analysis

To characterize key contributions to the observed encoding field fluctuations, we performed principal component analysis (PCA) (24) of the phase coefficients and the reconstructed images. PCA identifies those orthogonal data components that capture most of the data variance. To the degree that independent mechanisms of perturbation give rise to orthogonal variation, PCA separates the effects of these mechanisms and determines their relative magnitude. In particular, if variance is concentrated along few principal components, PCA gives an indication of the number of relevant underlying processes and their reproducibility (25).

The principal components were computed by eigendecompositions of the individual data covariance matrices with entries $COV^{l}_{\kappa,\kappa'}$ for each phase coefficient $k_0(t)$, $k_x(t)$, and $k_y(t)$.

$$COV^{l}_{\kappa,\kappa'} = \frac{1}{N_\tau - 1}\sum_{\tau=1}^{N_\tau}\left(k_{l,\tau}(t_\kappa) - \overline{k_l}(t_\kappa)\right)\cdot\left(k_{l,\tau}(t_{\kappa'}) - \overline{k_l}(t_{\kappa'})\right), \quad [5]$$

where $\tau$ is the scan number, $\kappa$ the time index during each readout, $l = 0$, $x$, $y$, and the bar indicates the mean over $N_\tau = 9 \times 400$ scans.

The principal components are ordered according to the amount of variance they explain. The first principal component explains most of the variance in the data, the second principal component the second most variance, and so on. In a second step, the temporal evolution of these characteristic readout time courses, i.e. principal components, over all $N_\tau$ scans is assessed by projection of the mean-corrected phase coefficient data onto each principal component:

$$proj_{\delta,l}(t_\tau) = \sum_{\kappa} PC_{\delta,l}(t_\kappa)\cdot\left(k_{l,\tau}(t_\kappa) - \overline{k_l}(t_k)\right), \quad [6]$$

where $\delta$ is the number of the respective principal component. Each projection reflects how the contribution of the respective principal component changes over scans, and thus provides a picture of the fluctuation patterns over time.

To characterize typical image fluctuations induced by field fluctuations, we performed PCA on the image time series containing fluctuations in $k_0(t)$ and $\boldsymbol{k_{x,y}}(t)$, respectively. This yielded principal components in the image domain and their corresponding projections, which reflected the evolution of image fluctuations over time. Because the phantom was placed at a slightly different position on each day, the PCA on the images was performed separately for each day.

## RESULTS

A close review of the effects of fluctuations in $k_0$ and $\boldsymbol{k_{x,y}}$ on the image time series emphasizes the characteristic fluctuations in EPI time series introduced by incomplete knowledge of encoding field fluctuations, as is typically the case for standard image reconstruction on commercial MRI systems. First, we compare the case where full monitoring information (reconstruction scheme 1) was employed in the image reconstruction versus no concurrent monitoring information (reconstruction scheme 2; Fig. 1C,D). Low SD values within the phantom and little ghosting was observed in the reference reconstruction (Fig. 1C). In contrast, fluctuations in $k_0$ and $\boldsymbol{k_{x,y}}$ induced ghosting and high SD values at the boundaries of the object (Fig. 1D). Here we analyze the influence of different field fluctuations on the image time series.

### Image Accuracy and Precision Losses Induced by Field Fluctuations

First, we considered the effect of $k_0$ fluctuations (reconstruction scheme 3; Table 2) on the image time series using the measured coil data (Fig. 2). The SD values were scaled to the maximum intensity value of the mean image reconstructed using the concurrently monitored phase coefficients. The SD image, characterizing the spatial fluctuation pattern, depicted fluctuations in the image that were especially high at the edges of the object (Fig. 2A) (maximum SD, 31.3%; mean SD, 1.0%). The RMSE, which depicted the temporal fluctuation pattern, showed a characteristic temporal evolution with a large dynamic range (Fig. 2B) (maximum RMSE, 10.8%; mean RMSE, 4.7%). The minimum is located in the central part of set 1, where the actual global phase evolution during image acquisition corresponds to the mean $k_0$ used for image reconstruction (Fig. 3A). Hence, the image deviations were very small. However, scans obtained earlier or later than this instance exhibited considerable image deviations. In comparison, the RMSE of the image time series reconstructed using the concurrently monitored phase coefficients (reconstruction scheme 1) is much lower and less variable (maximum RMSE, 0.6%; mean RMSE, 0.3%) (Fig. 4B). Equivalently, the fluctuations are reduced as verified by the low SD (maximum SD, 1.2%; mean SD, 0.3%) (Fig. 1C).

Second, we evaluated the effect of $\boldsymbol{k_{x,y}}$ fluctuations on the image time series (reconstruction scheme 4). We observed ghosting artifacts that compromised the image precision locally (maximum SD, 2.0%; mean SD, 0.4%) (Fig. 4A). The RMSE showed a similar temporal evolution on days 1 and 2 in all sets. The data sets of day 3 did not show such a correspondence; only a general decrease of the RMSE was observed (maximum RMSE, 1.5%; mean RMSE, 0.6%) (Fig. 4B).

For $k_0$ as well as $\boldsymbol{k_{x,y}}$, the observed image time series fluctuations from the measured coil data could be reproduced, in terms of both quantity and quality, on simulated coil data (Figs. 2C,D and 4C,D). This result indicates that transmit/receive chain and object fluctuations can be excluded as mechanisms for the observed fluctuations.

Likewise, the field monitoring measurement itself constitutes no relevant source of image fluctuations. Both the SD and RMSE of the image time series disturbed solely by probe phase noise were one order of magnitude lower than observed effects due to fluctuations in $k_0$ and $\boldsymbol{k_{x,y}}$ (Figs. 2E,F and 4E,F). Furthermore, the observed fluctuation patterns in the images were qualitatively different from image fluctuations due to encoding field fluctuations.

In summary, we observed in phantom experiments that accuracy and precision in image time series suffered considerably from field fluctuations, resulting in SD values up to 31.3% in $k_0$ and 2.0% in $\boldsymbol{k_{x,y}}$.

### Fluctuations of the Global Phase and Trajectory

Depicting the measured phase coefficients for all scans of set 1 (slice 9), we found fluctuations in the encoding fields at different orders of magnitude for distinct phase coefficients (Figs. 3 and 5). Specifically, for $k_0$ (Fig. 3), the main fluctuation over scans were an increasing slope of the linear component (Fig. 3A). This is even more conspicuous after subtracting the mean of the time series (Fig. 3C).

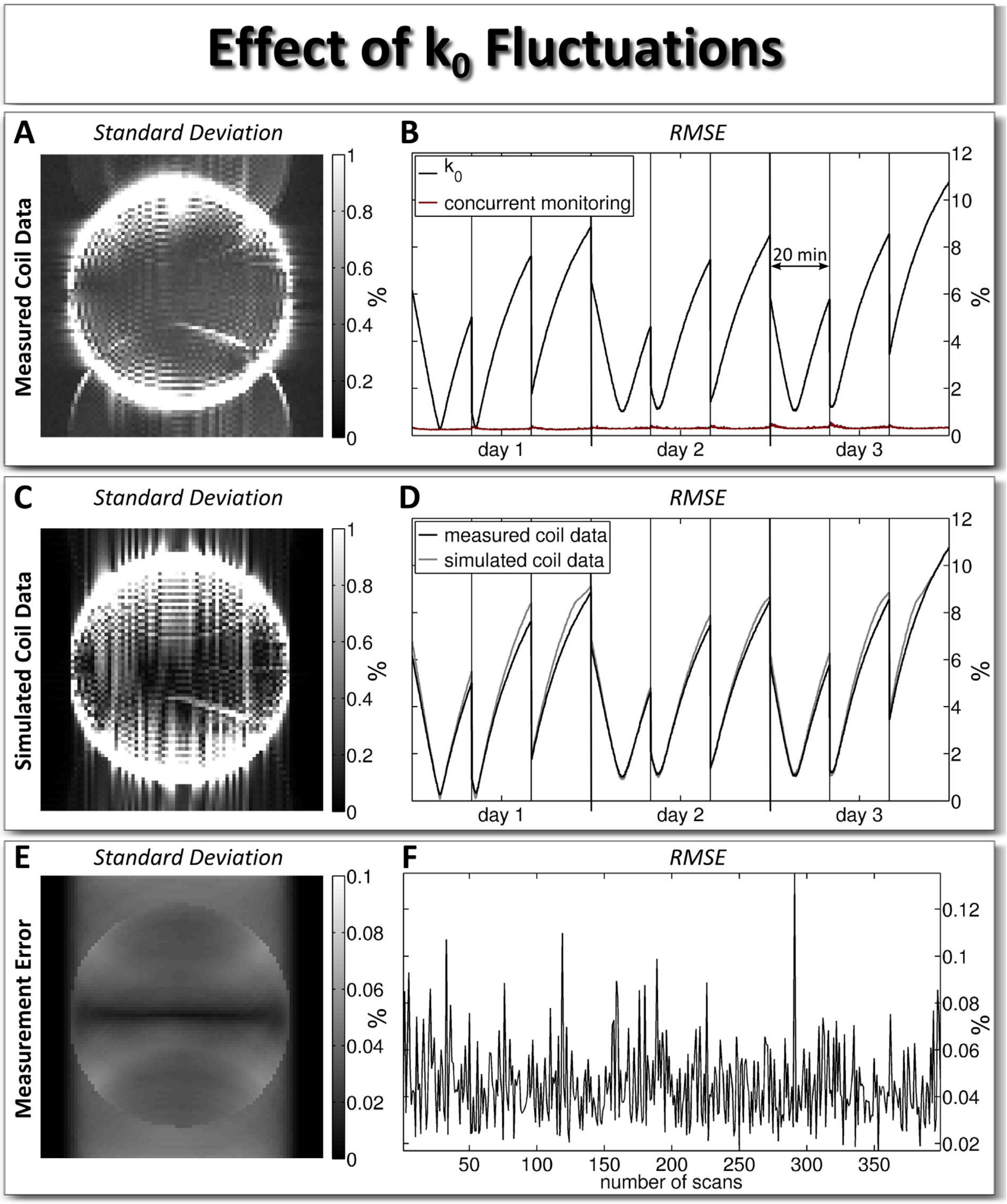


FIG. 2. Effect of $k_0$ fluctuations (reconstruction scheme 3). The image time series is scaled such that the mean image is in the range [0, 1]. The SD images depict the percent signal change in image intensity. **A:** SD image depicting the effects of $k_0$ fluctuations (set 1, slice 9). **B:** RMSE of the image time series affected by $k_0$ fluctuations in black (slice 9). RMSE of the reference image time series reconstructed using the concurrently monitored phase coefficients in red. **C:** SD image using simulated coil data and an identical reconstruction scheme as above. **D:** RMSE of the image time series affected by $k_0$ fluctuations using simulated coil data. **E, F:** SD image and RMSE characterizing the influence of probe phase noise in $k_0$ on the image time series.

Furthermore, by indicating the SD of the probe noise determined in a separate experiment (cf. noise in probe readouts), the high sensitivity of the measurement setup was illustrated: actual $k_0$ fluctuations between subsequent readouts were higher than the probe phase noise (Fig. 3B). For $k_x$ (Fig. 5A) and $k_y$ (Fig. 5C), the observed fluctuations were small compared to the dynamic range of the EPI trajectory (0.5‰ and 2‰, respectively). However, a complex

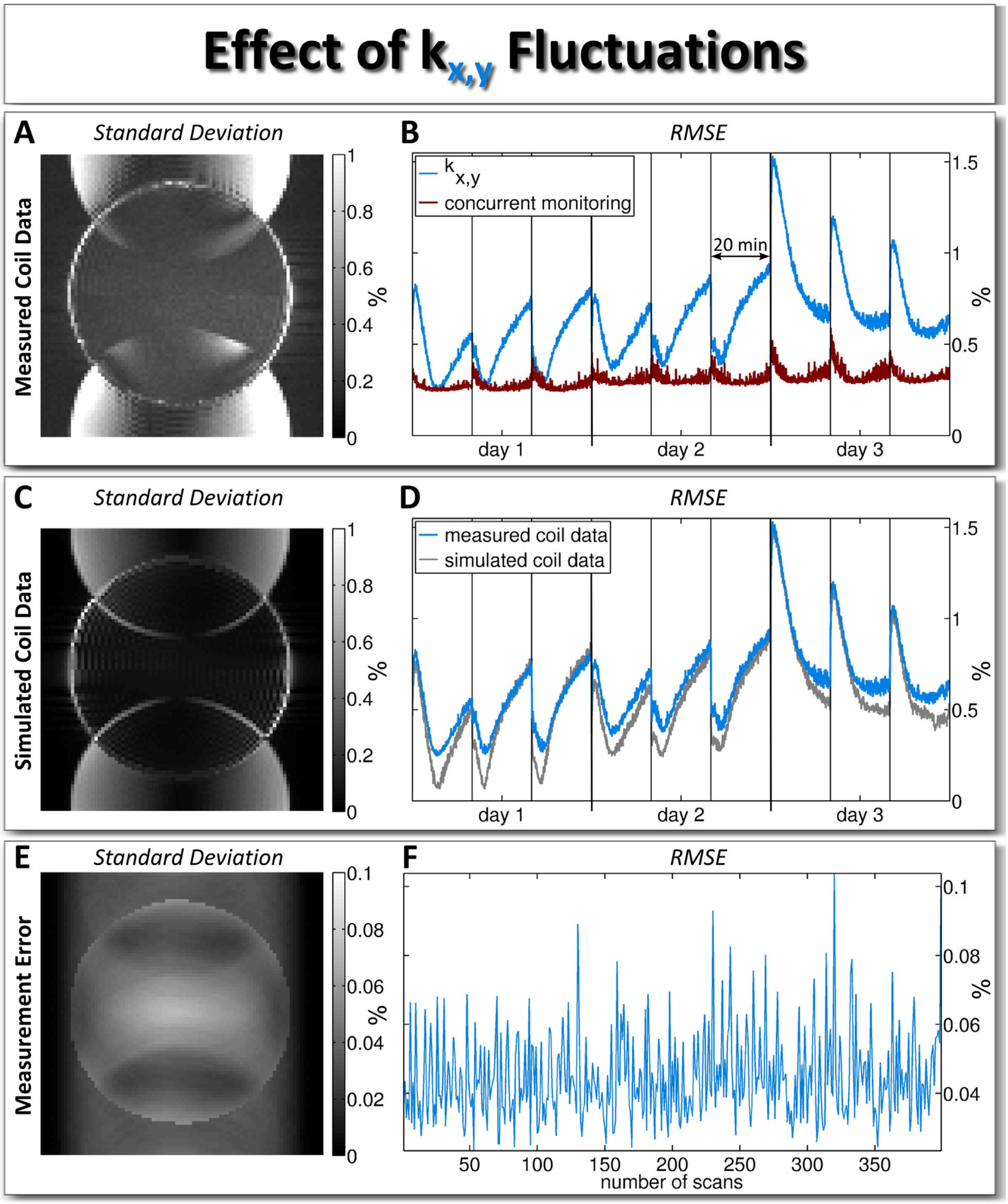


FIG. 3. Effect of $\boldsymbol{k_{x,y}}$ fluctuations (reconstruction scheme 4). The image time series is scaled such that the mean is in the range [0, 1]. The SD images depict the percent signal change in image intensity. **A:** SD image depicting the effects of $\boldsymbol{k_{x,y}}$ fluctuations (set 1, slice 9). **B:** RMSE of the image time series affected by $\boldsymbol{k_{x,y}}$ fluctuations in black (slice 9). RMSE of the reference image time series reconstructed using the concurrently monitored phase coefficients in red. **C:** SD image using simulated coil data and an identical reconstruction scheme as above. **D** RMSE of the image time series affected by $\boldsymbol{k_{x,y}}$ fluctuations using simulated coil data. **E, F:** SD image and RMSE characterizing the influence of probe phase noise in $\boldsymbol{k_{x,y}}$ on the image time series.

fluctuation scheme is present in $k_y$ (readout direction), exhibiting a dominant high-frequency modulation at approximately the EPI readout frequency, which can be detected clearly with the given setup sensitivity (Fig. 5D). The complex temporal structure of the observed field fluctuations necessitated dimensionality reduction using PCA.

PCA characterized the phase coefficient fluctuations on different time scales. While the principle components

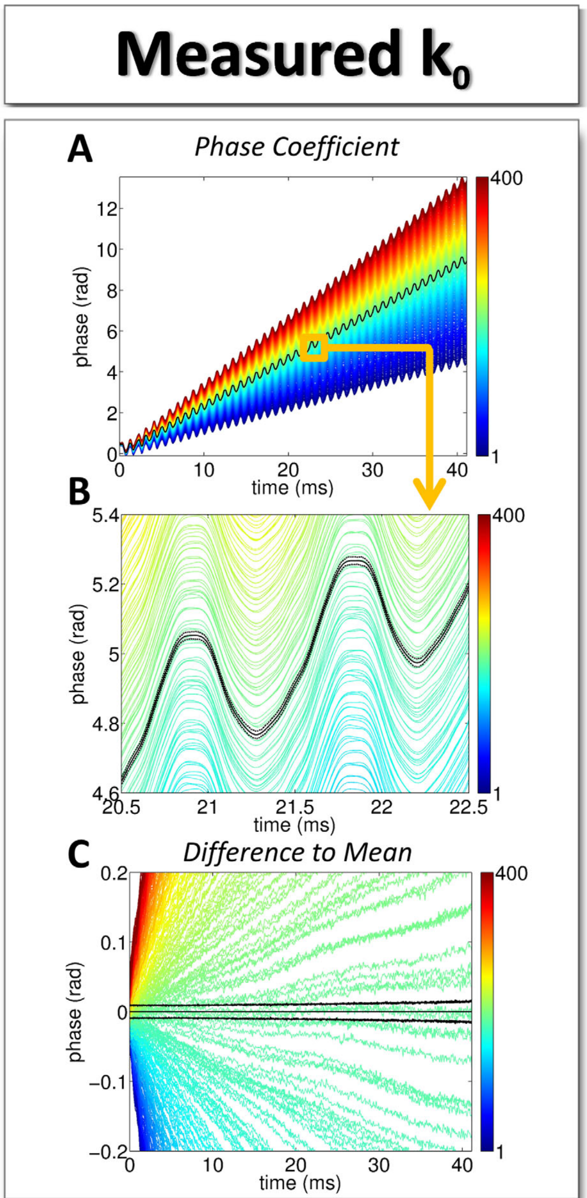


FIG. 4. Measured $k_0$. **A:** Evolution of phase coefficient $k_0$ during single-shot EPI readouts (set 1, slice 9). The color coding indicates the scan index within one session (blue = 1, red = 400). **B:** Zoom depicting the mean of phase coefficient $k_0$ in black ± the SD of the setup noise in dotted black. **C:** Difference of the measured phase coefficient $k_0$ and its mean. The ± SD of the setup noise is given in black.

themselves represent fluctuations within a readout, their corresponding projections enable following fluctuation dynamics between readouts (i.e., within each session, between sessions, and between days). We observed only few effects driving the variability between all scans in all sets (Fig. 6). In all three phase coefficients, the first principal component explained more than 80% of the variance.

For $k_0$, the first principal component (explaining 99.98% of the variance) constituted a linear phase increase within each readout (Fig. 6A). The corresponding projection, i.e. slope of the linear term, reflected a drift in the static $B_0$-field over readouts, since a constant offset in the $B_0$-frequency induces a linear phase in $k_0$. The projections showed temporal characteristics of a heating process, exhibiting a smooth increase of diminishing slope. The dynamic range within one set was about 30 Hz field offset. The same pattern emerged on each day, though variable offsets occurred between sessions and days (Fig. 6B).

The PCA of $k_x$ yielded a first principal component (84.6% of explained variance) containing a superposition of a linear increase and a modulation around the EPI readout frequency (Fig. 6C). Interestingly, although the component itself had distinct features, the projection was relatively noisy and did not show a reproducible temporal pattern across sets (Fig. 6D). The first component of $k_y$ (85% of explained variance) exhibited a linear increase and modulation similar to that for $k_x$ (Fig. 6E). The corresponding projection showed a linear decrease over time and considerable fluctuations on the time scale of seconds (Fig. 6F). These fluctuations do not stem from probe phase noise. We evaluated the variance in the PCA projections originating from probe phase noise using propagation of uncertainty (26); the standard deviation in the first projection in $k_y$ is more than one order of magnitude smaller than the observed fluctuations in the projection over seconds.

For $k_y$, the second principal component also explained a significant proportion of the total variance (12.1%). Furthermore, it showed a distinct structure both in the principal component itself and its projection: Again, an oscillation approximately at the EPI frequency was the dominating pattern within the principal component, with a slow amplitude modulation indicative of a beat phenomenon (Fig. 6G). The evolution of the projection showed heating characteristics similar to $k_0$, which were fairly reproducible in every set (Fig. 6H).

### Analysis of Image Fluctuations using Image PCA

We used PCA to characterize image fluctuations induced by $k_0$ and $\boldsymbol{k_{x,y}}$ fluctuations (reconstruction schemes 3 and 4) for each day separately (Fig. 7). Fluctuations in the encoding fields induced few strong effects (64%–81% explained variance) and the principal components were stable over different days. Fluctuations in $k_0$ induced a downward shift of about one pixel in one session (Fig. 7A). The projection was smooth and reproducible on each day (Fig. 7B). Fluctuations in $\boldsymbol{k_{x,y}}$ induced mainly an N/2 ghosting artifact and, additionally, a slight horizontal edge in the center of the image (Fig. 7C). Again, the projection had the same time course on each day and was slightly noisier compared to $k_0$ (Fig. 7D).

### Reproducibility of Field Fluctuations for Calibration

Based on the results of the phase coefficient PCA, where we found the same characteristic fluctuations in each set and projections with similar dynamics, we investigated the feasibility of a session calibration approach (Table 2) to reduce image fluctuations induced by field fluctuations (Fig. 8). Image fluctuations due to non-reproducible

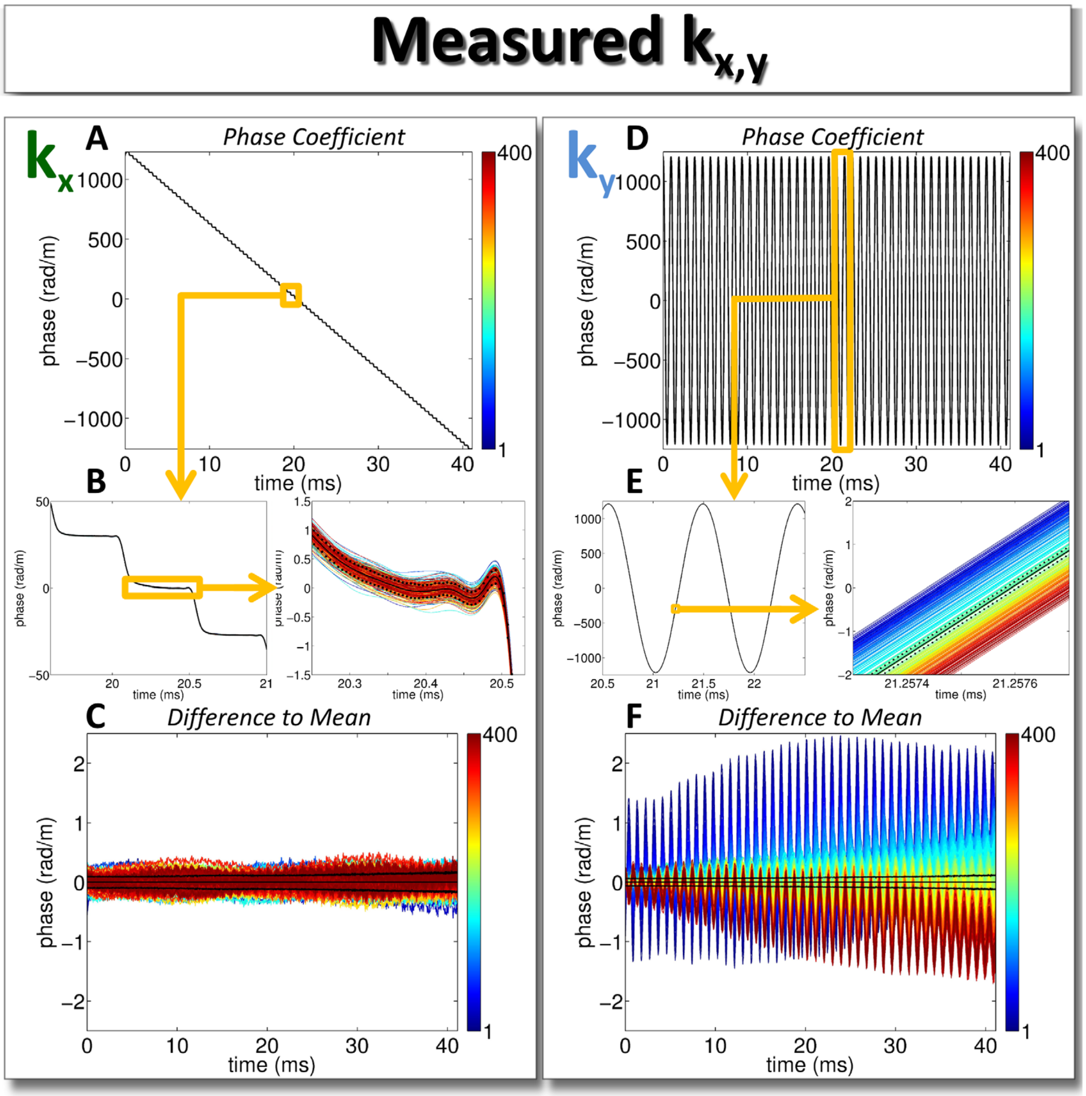


FIG. 5. Measured $\boldsymbol{k}_{x,y}$. **A, D:** Evolution of phase coefficient $k_x$ (phase encoding, A) and phase coefficient $k_y$ (frequency encoding, D) during single-shot EPI readouts (set 1, slice 9). The color coding indicates the scan index within one session (blue = 1, red = 400). **B, E:** Zoom depicting the mean of phase coefficient $k_x$ (B) and $k_y$ (E) in black ± the SD of the setup noise in dotted black. **C, F:** Difference of the measured phase coefficient $k_x$ (C) and $k_y$ (F) and their means, respectively. The ±SD of the setup noise is given in black.

effects, e.g., history-dependent and random phase coefficient fluctuations, could only be corrected for via concurrent magnetic field monitoring (Fig. 8A). Using reconstruction scheme number 5 (i.e., session calibration for $k_0$), the SD compared to the reference reconstruction was increased, especially at the edges of the object (maximum SD, 9.1%; mean SD, 0.4%) (Fig. 8B). Between sessions of the same day, the RMSE increased, approaching nearly 10 times the values found in the concurrent monitoring case (maximum RMSE, 8.6%; mean RMSE, 4.4%) (Fig. 8D). Between days, the RMSE was lowest in corresponding sessions and had reduced dynamics. However, an offset of up to 2% (i.e., on the order of expected BOLD effect sizes) remained.

In contrast, the SD images obtained by reconstruction scheme number 6 (i.e., session calibration in $\boldsymbol{k}_{x,y}$) were comparable to the concurrent monitoring case (maximum SD, 1.2%; mean SD, 0.3%) (Fig. 8C). However, the RMSE increased from day 1 to day 2 and from day 2 to day 3, indicating an accuracy loss with its maximum in set 7 at triple the amount of RMSE (maximum RMSE, 1.0%; mean RMSE, 0.6%) (Fig. 8D).

## DISCUSSION

In this study, we measured and characterized encoding field fluctuations in EPI time series in the global phase $k_0$ as well as the trajectory $\boldsymbol{k}_{x,y}$, which induced substantial image fluctuations in the range of the BOLD effect. Fluctuations in $k_0$ led to precision (SD up to 31%) and accuracy losses (RMSE up to 11%) chiefly due to variable pixel shifts. Fluctuations in $\boldsymbol{k}_{x,y}$ induced ghosting artifacts with SD values up to 2% and RMSE values up to 1.5%. Concurrent magnetic field monitoring reduced

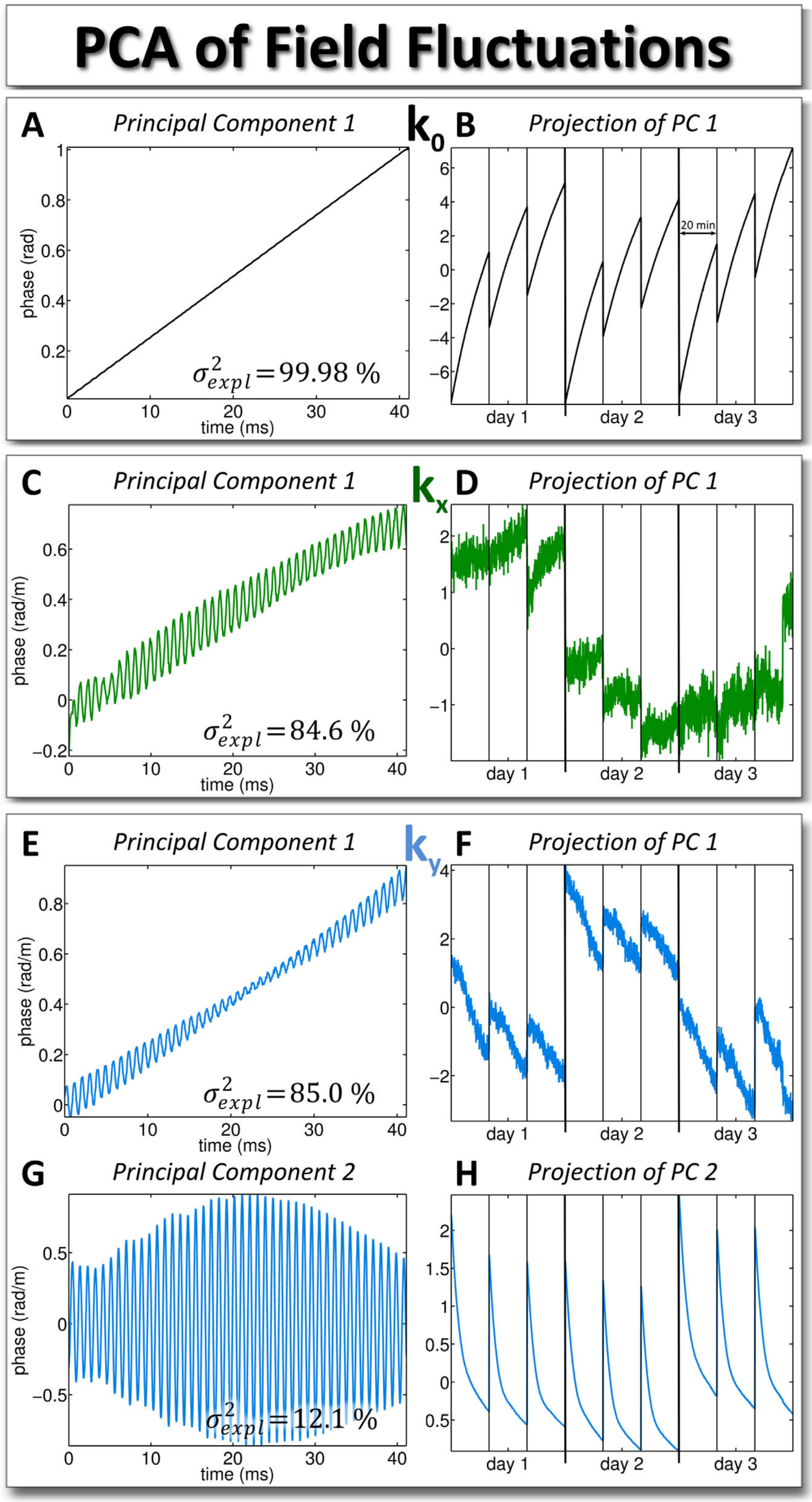


FIG. 6. PCA of field fluctuations. **A, B:** Principal component 1 (A) and the corresponding projection of phase coefficient $k_0$ (B). A projection change of 1 corresponds to a field drift of 3.9 Hz (1 rad/41.1 ms), given the normalization of the slope of PC 1. **C, D:** Principal component 1 (C) and the corresponding projection of phase coefficient $k_x$ (D). **E–H:** Principal component 1 and 2 (E and G) and the corresponding projections of phase coefficient $k_y$ (F and H). A projection change of 1 corresponds to a field drift of 3.9 Hz/m (1 rad/m/41.1 ms), given the normalization of the slope of PC 1.

the fluctuations in the EPI time series substantially (SD up to 1.2%, RMSE up to 0.6%) and removed temporally correlated image fluctuations. This capability holds promise for resting state fMRI, where spurious correlation patterns are especially confounding. Likewise, for task-based fMRI, the increased sensitivity and accuracy afforded by field monitoring may improve effect detection and localization. In further work, these benefits will need to be compared with the performance of alternative means of data correction, particularly with image-based

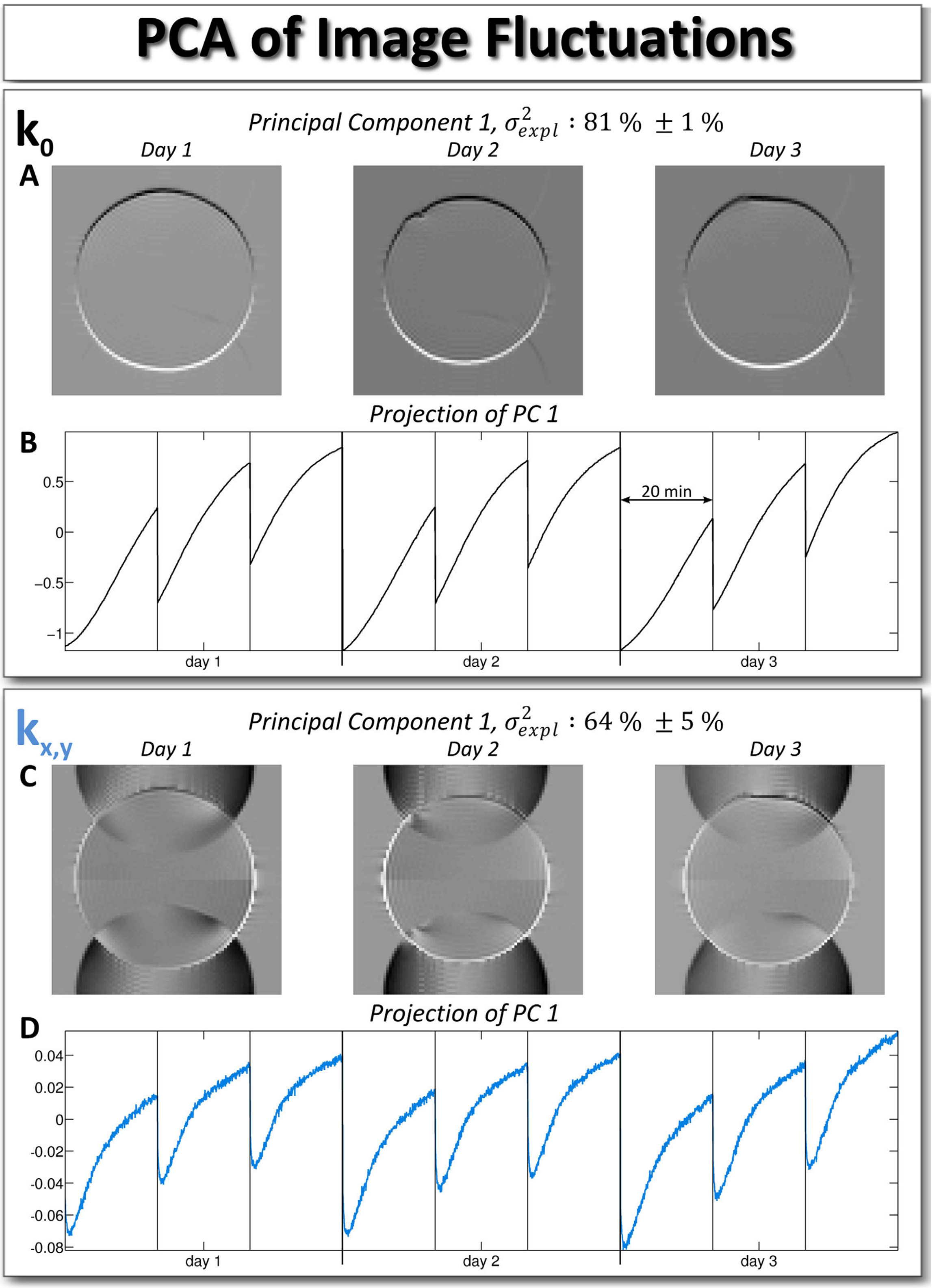


FIG. 7. PCA of image fluctuations. **A, B:** Principal component 1 (A) and the corresponding projections (B) of the image time series affected by $k_0$ fluctuations (reconstruction scheme 3), separated for each day. The Principal Components were scaled to the same dynamic range as the mean image. **C, D:** Principal component 1 (C) and the corresponding projections (D) of the image time series affected by $\boldsymbol{k_{x,y}}$ fluctuations (reconstruction scheme 4), separated for each day.

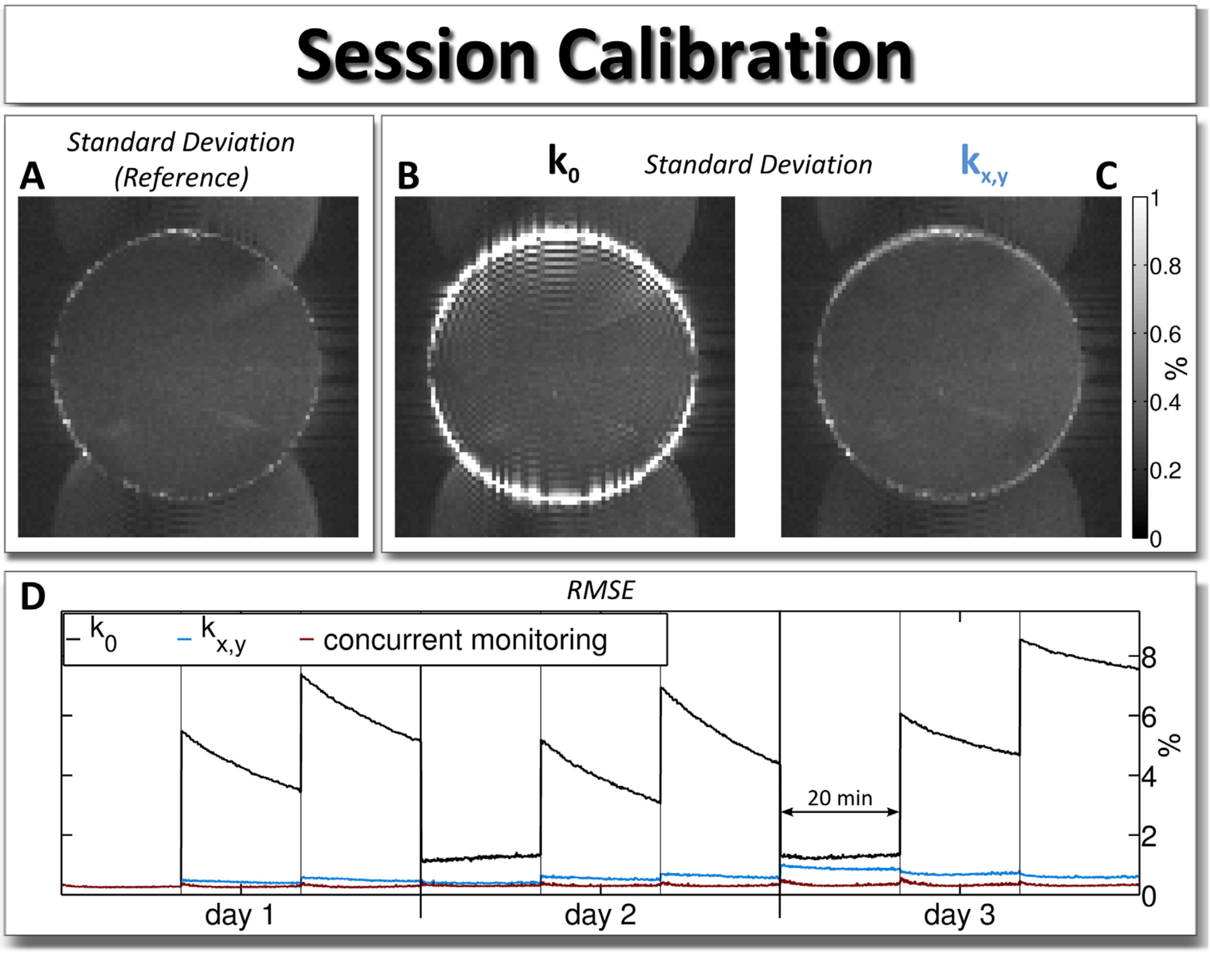


FIG. 8. Session calibration. **A:** SD image using reconstruction scheme 1, i.e. concurrently monitored phase coefficients (set 1, slice 9). **B, C:** SD images using a session calibration approach for $k_0$ (reconstruction scheme 5, B) or $\boldsymbol{k_{x,y}}$ (reconstruction scheme 6, C) (set 2, slice 9). **D:** RMSE of the reconstructed images obtained by the three reconstruction schemes ($k_0$ fluctuations in black, $\boldsymbol{k_{x,y}}$ fluctuations in blue, concurrent monitoring in red).

realignment. Realignment primarily targets motion during fMRI studies but also captures bulk image shifts in EPI due to field drifts. However, current realignment procedures are mostly based on three-dimensional rigid-body registration, which does not account for shifts that vary between slices. Realignment also does not address image errors other than shifts, such as ghosting. Further frequently used means of addressing data biases include high-pass filtering, which will also remove slow signal variation of interest, particularly in resting state fMRI.

As seen, concurrent magnetic field monitoring provides a comprehensive means to correct for field fluctuations in image time series. This also indicates that the reported field changes indeed affect the imaged object and are not mere artifacts of the measurement setup. Furthermore, the high congruency between measured and simulated coil data showed that image fluctuations observed in the experiment were caused predominantly by fluctuations in encoding fields of zeroth and first spatial order. Higher-order field fluctuations require further investigation. Their impact on image fluctuations can be assessed and corrected by more advanced reconstruction algorithms (19). Fluctuations in the magnetization and detection sensitivity due to instabilities in the transmit/receive chains contributed less to image fluctuations. The potential concern of gradient-induced mechanical vibration of the field probe setup, which will cause slight error in the field measurement, remains to be investigated.

We characterized the effects of a typical EPI time series schedule on system-related encoding field fluctuations via principal component analysis. Herein, we observed only a few strong effects driving field variability. The fluctuations in $k_0$ were nearly exclusively explained by a linear phase increment in the first principal component, reflecting a change in the global $B_0$ field. The projection of this component showed slow drift dynamics over scans of a session approaching saturation, with an overall range of 30 Hz, in line with literature describing heating effects on magnets, gradients, and shims (5). However, because dynamic $f_0$ correction and the cold head were turned off in our experiments, the magnitude of these field drifts may vary in practice, depending on vendor-specific correction methods. The fluctuations in $k_x$ (i.e., in the phase-encoding direction) were small, on the order of the sensitivity of our monitoring setup (0.1 rad/m). They exhibited two prominent features in their principal components: a linear phase increment and an oscillation at and around the EPI readout frequency. The evolution of this fluctuation followed no clear trend over scans and appeared to be noisy. Thus, the physical causes of these fluctuation patterns remain speculative. The fluctuations in $k_y$, the frequency-encoding direction, were dominated by two principal components with features already observed in $k_x$: a linear phase increment in the first principal component, and an oscillation at and around the EPI readout frequency in both components. The linear phase increment of the first principal component in $k_y$ reflects an offset in the gradient field. The modulation with the EPI frequency in both relevant principal components in $k_y$ might reflect a delay as well as a slight shift in the EPI frequency. For the first component, the projection again seemed to be noisy on the order of seconds. These seemingly random fluctuations could not be attributed to measurement noise, which was verified by propagation of uncertainty (26) using the independently measured probe phase noise statistics. Over the course of a full session, the projection exhibited an overall slow linear decrease. In addition, the projection of the second principal component exhibited slow dynamics over a session, which are similar to the temporal characteristics of the projections in $k_0$, again indicating a thermal mechanism. Heating of gradient coils is associated with slight shifts of their mechanical resonance frequencies (27), which is a plausible cause of the beat observed in the second principal component of $k_y$. Irrespective of the exact underlying mechanisms, the small number of significant principal components of fluctuation suggests that there may be scope for enhanced hardware models using system temperature as a key parameter.

In view of the significant hardware demands of concurrent field monitoring, simpler correction or even calibration methods to counteract field fluctuations might be conceivable given the limited amount of principal components in the fluctuations we observed and their apparently predictable projection behavior over sessions. With respect to calibration by field monitoring, we found the sole field dynamics of one session insufficient to calibrate field fluctuations in other sessions. Specifically, while the fluctuation patterns were qualitatively reproducible, several of their parameters varied between sessions. In particular, the global $B_0$ offset differed at the start of each session, depending on the heating history of the system. Consequently, strong image fluctuations (maximum SD, 9.1%; mean SD, 0.4%) remained despite calibration with the $k_0$ dynamics of another session. For $\boldsymbol{k}_{\mathbf{x,y}}$, the variation between sets was manifested predominantly in the offset and dynamic range of the projections. Therefore, the image accuracy decreased from day to day using session calibration. One could envisage that calibration methods might succeed if the reproducible behavior determined by magnetic field monitoring were complemented by a simpler measure of the variable parameters, such as navigators for the determination of the $f_0$ frequency offset or temperature measurements informing a model of the slow saturation dynamics that the projections of $k_0$ and $k_y$ reflect.

With respect to the generalizability of these results to other imaging sequences, such as spirals (28,29), we expect that high-duty cycle single-shot sequences will induce comparable system-related field fluctuations. This prognosis is based on the observed few readout fluctuation patterns and their recurrent dynamics in each session and on each day, which indicate system-immanent properties. The concrete manifestation of these fluctuations in the images, however, will depend on the acquisition parameters and the k-space trajectory itself. We observed a correspondence in the projections of field and image fluctuations. Based on this, we infer that the majority of image time series fluctuations (64%–81%) can be attributed to specific types of field fluctuations. However, there is no straightforward one-to-one mapping. We observed a correspondence of the projection of the second principal component of phase coefficient $k_y$ (Fig. 6H) and the projection of the first principal component of the reconstructed images influenced by fluctuations in $\boldsymbol{k}_{\mathbf{x,y}}$ (Fig. 7D). Despite the first principal component of phase coefficient $k_y$ captures the vast majority of the variance, the projections of the second principal component in $k_y$ matches better with the projection of the first principal component of the reconstructed images. Hence, we conclude that the distribution of the fluctuations in k-space play a central role.

## CONCLUSION

In this study, we considered field fluctuations in phantom experiments and simulations to isolate the system-related field effects and establish their nonnegligible impact on image fluctuations. Similar investigations will need to be made in vivo, where physiological mechanisms such as breathing add to net field fluctuation in EPI time series.

## ACKNOWLEDGMENTS

We thank Klaas Enno Stephan for valuable feedback on the manuscript and Steffen Bollmann, David M. Cole, Jakob Heinzle, and Tina Wentz for discussing earlier versions. We also acknowledge Philips Healthcare for technical support, particularly Johan Overweg and Miha Fuderer for putting our findings in the perspective of the hardware involved.

## REFERENCES

1. Ogawa S, Lee TM, Kay AR, Tank DW. Brain magnetic resonance imaging with contrast dependent on blood oxygenation. Proc Natl Acad Sci U S A 1990;87:9868–9872.
2. Kwong KK, Belliveau JW, Chesler DA, Goldberg IE, Weisskoff RM, Poncelet BP, Kennedy DN, Hoppel BE, Cohen MS, Turner R. Dynamic magnetic resonance imaging of human brain activity during primary sensory stimulation. Proc Natl Acad Sci U S A 1992;89:5675–5679.
3. Börnert P, Schomberg H, Aldefeld B, Groen J. Improvements in spiral MR imaging. MAGMA 1999;9:29–41.
4. Addy NO, Wu HH, Nishimura DG. Simple method for MR gradient system characterization and k-space trajectory estimation. Magn Reson Med 2012;68:120–129.
5. Foerster BU, Tomasi D, Caparelli EC. Magnetic field shift due to mechanical vibration in functional magnetic resonance imaging. Magn Reson Med 2005;54:1261–1267.
6. De Zanche N, Barmet C, Jurek, Pruessmann KP. NMR probes for measuring magnetic fields and field dynamics in MR systems. Magn Reson Med 2008;60:176–186.
7. Boesch C, Gruetter R, Martin E. Temporal and spatial analysis of fields generated by eddy currents in superconducting magnets: optimization of corrections and quantitative characterization of magnet/gradient systems. Magn Reson Med 1991;20:268–284.

8. Pfeuffer J, Van de Moortele P-F, Ugurbil K, Hu X, Glover GH. Correction of physiologically induced global off-resonance effects in dynamic echo-planar and spiral functional imaging. Magn Reson Med 2002;47:344–353.
9. Vannesjo SJ, Wilm BJ, Duerst Y, Gross S, Brunner DO, Dietrich BE, Schmid T, Barmet C, Pruessmann KP. Retrospective correction of physiological field fluctuations in high-field brain MRI using concurrent field monitoring. Magn Reson Med 2015;73:1833–1843.
10. Duerst Y, Wilm BJ, Dietrich BE, Vannesjo SJ, Barmet C, Schmid T, Brunner DO, Pruessmann KP. Real-time feedback for spatiotemporal field stabilization in MR systems. Magn Reson Med 2015;73:884–893.
11. Duyn JH, Yang Y, Frank JA, van der Veen JW. Simple correction method fork-space trajectory deviations in MRI. J Magn Reson 1998; 132:150–153.
12. Vannesjo SJ, Haeberlin M, Kasper L, Pavan M, Wilm BJ, Barmet C, Pruessmann KP. Gradient system characterization by impulse response measurements with a dynamic field camera. Magn Reson Med 2013;69:583–593.
13. Ward HA, Riederer SJ, Jack CR. Real-time autoshimming for echo planar timecourse imaging. Magn Reson Med 2002;48:771–780.
14. Splitthoff DN, Testud F, Hennig J, Speck O, Zaitsev M. Real-time prospective shim correction using self-referencing navigators. In Proceedings of the 15th Annual Meeting of ISMRM, Berlin, Germany, 2007. p. 985.
15. Splitthoff DN, Zaitsev M. SENSE shimming (SSH): a fast approach for determining $B_0$ field inhomogeneities using sensitivity coding. Magn Reson Med 2009;62:1319–1325.
16. Barmet C, Zanche ND, Pruessmann KP. Spatiotemporal magnetic field monitoring for MR. Magn Reson Med 2008;60:187–197.
17. Barmet C, De Zanche N, Bertram J. Wilm, Klaas P. Pruessmann. A transmit/receive system for magnetic field monitoring of in vivo MRI. Magn Reson Med 2009;62:269–276.
18. Barmet C, Wilm BJ, Pavan M, Katsikatsos G, Keupp J, Mens G, Pruessmann KP. Concurrent higher-order field monitoring for routine head MRI: an integrated heteronuclear setup. In Proceedings of the 18th Annual Meeting of ISMRM, Stockholm, Sweden, 2010. p. 216.
19. Wilm BJ, Barmet C, Pavan M, Pruessmann KP. Higher order reconstruction for MRI in the presence of spatiotemporal field perturbations. Magn Reson Med 2011;65:1690–1701.
20. Pruessmann KP, Weiger M, Börnert P, Boesiger P. Advances in sensitivity encoding with arbitrary k-space trajectories. Magn Reson Med 2001;46:638–651.
21. Jackson JI, Meyer CH, Nishimura DG, Macovski A. Selection of a convolution function for Fourier inversion using gridding [computerised tomography application]. IEEE Trans Med Imaging 1991;10:473–478.
22. Beatty PJ, Nishimura DG, Pauly JM. Rapid gridding reconstruction with a minimal oversampling ratio. IEEE Trans Med Imaging 2005;24: 799 –808.
23. Gallichan D, Robson MD, Bartsch A, Miller KL. TREMR: Table-resonance elastography with MR. Magn Reson Med 2009;62:815–821.
24. Pearson K. On lines and planes of closest fit to systems of points in space. Philos Mag 1901;2:559–572.
25. Shlens J. A Tutorial on Principal Component Analysis. 2009. arXiv:1404.1100.
26. Ku HH. Notes on the use of propagation of error formulas. Gaithersburg, MD: National Bureau of Standards; 1966.
27. Busch J, Vannesjo SJ, Barmet C, Pruessmann KP, Kozerke S. Analysis of thermal stability of background phase errors in phase-contrast flow imaging. In Proceedings of the 21st Annual Meeting of ISMRM, Salt Lake City, Utah, USA, 2013. p. 69.
28. Ahn C, Kim J, Cho Z. High-speed spiral-scan echo planar NMR imaging .1. IEEE Trans Med Imaging 1986;5:2–7.
29. Glover GH, Lai S. Self-navigated spiral fMRI: interleaved versus single-shot. Magn Reson Med 1998;39:361–368.